

# Effects of magnetic field profile near anode on ion acceleration characteristics of a diverging magnetic field electrostatic thruster

D. Ichihara, A. Iwakawa, and A. Sasoh

Citation: [Journal of Applied Physics](#) **122**, 043302 (2017);

View online: <https://doi.org/10.1063/1.4995286>

View Table of Contents: <http://aip.scitation.org/toc/jap/122/4>

Published by the [American Institute of Physics](#)

---

## Articles you may be interested in

[Electrostatic/magnetic ion acceleration through a slowly diverging magnetic nozzle between a ring anode and an on-axis hollow cathode](#)

[AIP Advances](#) **7**, 065204 (2017); 10.1063/1.4985380

[Conducting wall Hall thrusters in magnetic shielding and standard configurations](#)

[Journal of Applied Physics](#) **122**, 033305 (2017); 10.1063/1.4995285

[Tutorial: Physics and modeling of Hall thrusters](#)

[Journal of Applied Physics](#) **121**, 011101 (2017); 10.1063/1.4972269

[Determination of plasma impedance of microwave plasma system by electric field simulation](#)

[Journal of Applied Physics](#) **122**, 043303 (2017); 10.1063/1.4993902

[Effect of anode position on the performance characteristics of a low-power cylindrical Hall thruster](#)

[Physics of Plasmas](#) **24**, 063518 (2017); 10.1063/1.4986091

[A multifunctional plasma and deposition sensor for the characterization of plasma sources for film deposition and etching](#)

[Journal of Applied Physics](#) **122**, 044503 (2017); 10.1063/1.4995278

---



# SciLight

Sharp, quick summaries **illuminating**  
the latest physics research

Sign up for **FREE!**



# Effects of magnetic field profile near anode on ion acceleration characteristics of a diverging magnetic field electrostatic thruster

D. Ichihara,<sup>a)</sup> A. Iwakawa, and A. Sasoh

*Department of Aerospace Engineering, Nagoya University, Nagoya, Aichi 464-8603, Japan*

(Received 21 March 2017; accepted 9 July 2017; published online 25 July 2017)

In this study, we investigated the effects of the magnetic field profile near a ring anode on the ion acceleration characteristics of a diverging magnetic field electrostatic thruster. In an examined electrostatic thruster, a diverging magnetic field is applied in the ion acceleration region, which comprises a ring anode and an insulating plate in the upstream and an off-axis hollow cathode in the downstream. The ionization near the ring anode inner surface is enhanced by increasing the axial magnetic field in the interior of the ring anode to 250 mT, thereby increasing the effective voltage for the ion acceleration. By supplying 0.41 mg/s argon gas as the working gas through a circular slit between the ring anode and the insulating plate, with a discharge voltage of 200 V, the working gas is almost fully ionized and accelerated to an average energy of 190 eV with a beam diverging angle of 39°. *Published by AIP Publishing.* [<http://dx.doi.org/10.1063/1.4995286>]

## I. INTRODUCTION

The implementation of electric propulsion in space applications, such as altitude control and orbit rising, is currently expanding owing to its associated high exhaust speed, which yields a high payload ratio.<sup>1</sup> In particular, thrusters using electrostatic acceleration, such as ion thrusters and Hall thrusters, are predominantly utilized owing to their high thrust efficiency in the specific impulse range of 1500 s and even higher.<sup>2</sup> In an ion thruster, an ion acceleration potential is applied using grid electrodes. The ion beam is collimated in the direction of the thrust through the grids. Because such ion acceleration processes are not associated with particle collisions, a high thrust efficiency, which is higher than 70%, is obtained.<sup>3</sup> However, the corresponding thrust density exhibits a maximum because of the Child-Langmuir space charge limit.<sup>4,5</sup> In a stationary-plasma-thruster (SPT)-type Hall thruster,<sup>2</sup> which is currently predominantly utilized in high-power space applications, the ion acceleration potential is maintained in the axial direction by electrons moving in a closed loop in the azimuthal direction under a radial magnetic field.<sup>6</sup> However, in practice, the applied magnetic field is curved so that the accelerating electric field exhibits an unfavorable radial component, thereby leading to collisions against the insulator walls in the acceleration channel.<sup>7</sup> In the past few decades, intensive investigations were performed for modifying the ion beam optics in Hall thrusters.<sup>8</sup> Mikellides *et al.*<sup>9</sup> proposed a concept named “magnetic shielding.” In this concept, ion collisions against the outer channel wall are mitigated by superimposing a magnetic field along the channel. Mazouffre *et al.*<sup>10</sup> proposed a “wall-less Hall thruster,” in which an anode is placed near the acceleration channel exit so that propellant ionization and acceleration occur outside the channel. However, ions diffused along the magnetic field and the beam optics was

deteriorated, thereby degrading the thrust performance compared to that of conventional Hall thrusters.<sup>11</sup> Cylindrical Hall thrusters,<sup>12</sup> high efficiency multistage plasma thrusters,<sup>13</sup> and cusped-field thrusters<sup>14</sup> have a cusped magnetic field so that the effective electric field for ion acceleration is radially inclined inward; thus, ion collisions against the channel wall are expected to be mitigated. Matlock<sup>15</sup> demonstrated that the diverging efficiency in the cusped-field thruster was enhanced using an external electromagnet.

Harada *et al.*<sup>16</sup> proposed the helicon electrostatic thruster (HEST), which comprised a unique electrode arrangement with a cusped magnetic field between a ring anode and a hollow cathode. Uchigashima *et al.*<sup>17</sup> reported that, in the HEST operation, the inner surface of the ring anode primarily acted as an electron collector. Ichihara *et al.*<sup>18</sup> were inspired by this result and proposed the diverging magnetic field electrostatic thruster (DM-EST), in which the ions were accelerated using the same electrodes and magnetic field as those of the HEST, but without the helicon plasma source. In an electrostatic accelerator, the kinetic energy of accelerated ions depends on the space potential difference from where the ions are generated to the downstream region. Generating ions near the anode potential region is important to utilize an applied voltage efficiently for ion acceleration. In order to generate ions near the anode, several methods and schemes were proposed. Foster *et al.*<sup>19</sup> proposed a “hollow anode scheme,” in which the propellant gas was injected through small holes on the anode surface of a magneto-plasma-dynamics (MPD) thruster so that ionization near an anode was enhanced and then the anode sheath drop was decreased. In the so-called “hollow anode plasma source,”<sup>20</sup> ionization is enhanced by decreasing the anode area so that the anode potential drop and anode sheath thickness are increased. In our previous study,<sup>18</sup> the effects of the working gas injection port on ion beam characteristics of the DM-EST were investigated. Injecting the working gas through an annular slit between the ring anode and the insulator enhanced the ionization near the ring anode inner surface because the local neutral number density was

<sup>a)</sup> Author to whom correspondence should be addressed: [ichihara@fuji.nuae.nagoya-u.ac.jp](mailto:ichihara@fuji.nuae.nagoya-u.ac.jp).

increased and, as a result, the probability of electron impact ionization was increased. The DM-EST has a similar magnetic field configuration and device geometry to the End-Hall ion source.<sup>21,22</sup> The End-Hall ion source (or thruster) comprises a diverging section in its anode. A conical “potential well” is formed over the anode inner surface so that the accelerated ions bounce back and forth against the well, and the extracted ion beams have a wide angular distribution. This configuration is suitable for plasma processing because it uniformly distributes ion beams over a large diverging angle. On the other hand, the anode of the DM-EST has a ring shape without a diverging section. The ring anode surface is exposed only in the short zone where efficient ionization of the propellant is expected to occur. Because the working gas is injected through the slit, neutrals primarily have an axial velocity and do not directly impinge against any wall in the downstream. The electrical potential distribution in the ion acceleration region is determined primarily by the magnetic field in the downstream region from the ring anode. The largest potential drop occurs near the end of the diverging magnetic field toward the axial direction. Such ion acceleration mechanisms are suitable for space propulsion. However, the effects of the magnetic field profile as well as the detailed mechanisms of ion acceleration in the DM-EST are still not well explored. In this study, the ion beam characteristics of the DM-EST are investigated by examining the magnetic field profiles through the measurement of the ion beam and plasma characteristics in the ion acceleration region.

## II. EXPERIMENTAL APPARATUS AND PROCEDURE

Figure 1 shows a schematic of the nominal configuration of the DM-EST which is examined in this study. The primary components, namely, the solenoid coil, ring anode, hollow cathode, and insulating channel walls, are the same as those investigated in Refs. 17 and 18. In this study, we introduced ring yokes fabricated using soft iron inside the

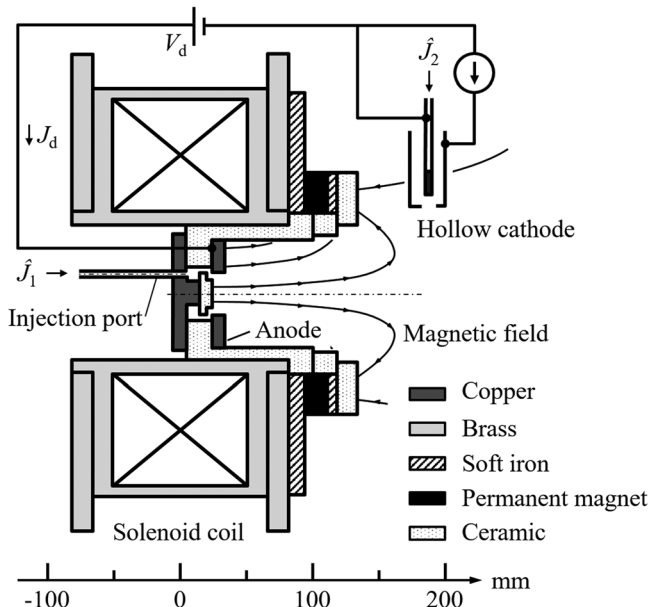


FIG. 1. Schematic of the DM-EST, “nominal” (N) configuration.

solenoid coil case for modifying the applied magnetic field profile inside the ring anode. A copper ring anode with an inner diameter of 27 mm and a thickness of 10 mm was located at 25 mm downstream from the coil center. An insulating plate fabricated using boron nitride was located inside the ring anode to plug the working gas in the acceleration channel. The working gas, argon, was injected through the 1.5-mm-thick circular slit along the anode inner surface. In this region, an axial magnetic field was applied parallel to the ring anode inner surface. In the downstream region, the magnetic field was considerably modified using Nd-Fe-B permanent magnets and soft iron yokes to generate a diverging magnetic field followed by a field-free region with the magnetic field strength lower than 3 mT. The orifice of a hollow cathode (DLHC-1000, Kaufman & Robinson, Inc.) was located at a radial position of 70 mm and an axial position of 175 mm downstream from the coil center.

In this study, four magnetic field profiles, types N, S, A, and C, were investigated, as shown in Fig. 2. Here, the cylindrical coordinates ( $r, z$ ) for the axisymmetric configuration, where  $r$  and  $z$  are the radial and axial coordinates, respectively, are defined on the central axis with their origin at the downstream surface of the insulating plate. The magnetic field strength  $B$  at the origin,  $B(0 \text{ mm}, 0 \text{ mm})$ , and at the exit of the annular slit,  $B(13.5 \text{ mm}, 0 \text{ mm})$ , was used for characterizing each magnetic field profile. In Type N [Fig. 2(a)], the inner support that backed the insulating plate was fabricated using copper. The magnetic field profile of Type N was the same as that used in Refs. 17 and 18. The magnetic field inside the ring anode was relatively uniform, that is,  $B(0 \text{ mm}, 0 \text{ mm}) = B(13.5 \text{ mm}, 0 \text{ mm}) = 100 \text{ mT}$ . In the other types shown in Figs. 2(b) to 2(d), the magnetic field profile near the ring anode was modified by changing the material of the inner and outer supports. In Type S [Fig. 2(b)], the magnetic field inside the ring anode was almost uniformly enhanced by using the inner and outer supports that were fabricated using soft iron. The length of the outer support at its inner-most portion was only 9 mm and was connected to another 9-mm-long cylinder fabricated using copper. The magnetic field strengths at both the center and the ring anode inner surface were increased within a variation of 10%, that is,  $B(0 \text{ mm}, 0 \text{ mm}) = 210 \text{ mT}$  and  $B(13.5 \text{ mm}, 0 \text{ mm}) = 190 \text{ mT}$ . In Type A [Fig. 2(c)], the insulating plate was backed by a copper inner support, which had the same shape as the inner support of Type S. The magnetic field was increased only near the ring anode inner surface by using an outer support fabricated using soft iron, which had its full length, without a copper extension cylinder, such as that used in Type S. The magnetic field was considerably enhanced near the ring anode inner surface ( $B(13.5 \text{ mm}, 0 \text{ mm}) = 250 \text{ mT}$ ) compared to that on the central axis ( $B(0 \text{ mm}, 0 \text{ mm}) = 150 \text{ mT}$ ). In Type C [Fig. 2(d)], the copper inner support was replaced by an inner support fabricated using soft iron with the same shape as that of Type S, and the outer support was fabricated using copper. The magnetic field was considerably enhanced near the central axis, with  $B(0 \text{ mm}, 0 \text{ mm}) = 300 \text{ mT}$  and  $B(13.5 \text{ mm}, 0 \text{ mm}) = 190 \text{ mT}$ .

The ion beam energy,  $E_i$ , was estimated from the ion beam energy distribution function (IEDF), which was

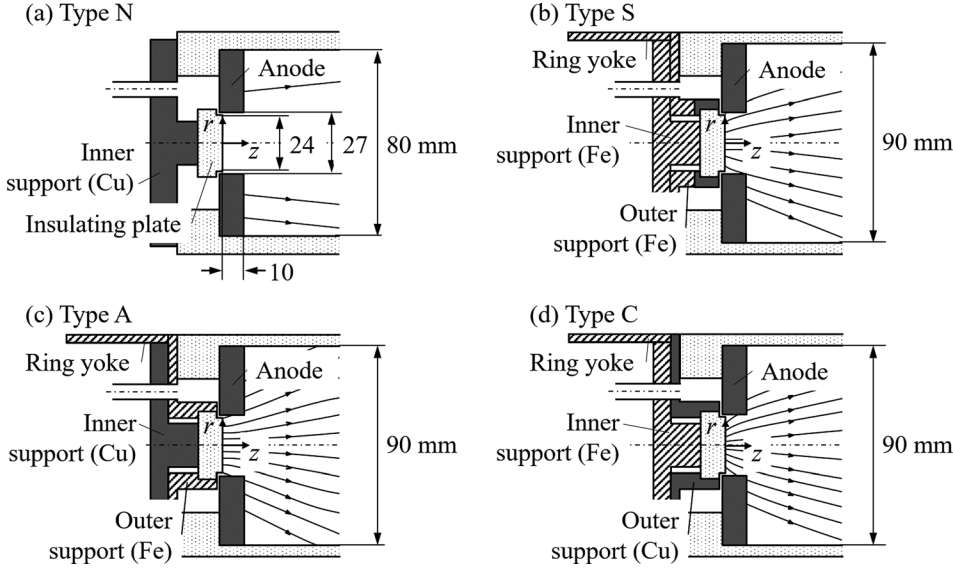


FIG. 2. Applied magnetic fields: (a) Type N, (b) Type S, (c) Type A, and (d) Type C.

measured using a retarding-potential analyzer (RPA).<sup>23</sup> The same RPA as in Ref. 16 was used. The RPA was fixed at  $(r, z) = (0 \text{ mm}, 350 \text{ mm})$ . The corrected ion current  $J_c$  was measured by varying the third grid potential of RPA  $V_{\text{RPA}}$  from  $-20 \text{ V}$  to  $440 \text{ V}$  with respect to the cathode potential. Figure 3 shows an example of the  $J_c$  variation and the calculated IEDF.  $J_c$  was normalized by a baseline value with  $V_{\text{RPA}} < 0$ . The normalized  $J_c$  was fitted to a superimposition of Gaussian functions using the least-squares method.<sup>16</sup> The IEDF was obtained by differentiating the fit curve with respect to  $V_{\text{RPA}}$ . The calculated IEDF comprised two distinct peaks at  $V_{\text{RPA}} = \phi_1$  and  $V_{\text{RPA}} = \phi_2$ . Using  $\phi_1$  and  $\phi_2$ ,  $E_i$  is estimated by

$$E_i \equiv \phi_2 - \phi_1. \quad (1)$$

In the case of Fig. 3,  $\phi_1 = 42 \text{ V}$ ,  $\phi_2 = 190 \text{ V}$ , and  $E_i = 148 \text{ eV}$ . Here, it should be noted that  $\phi_1$  did not equal the space potential. Due to charge exchange processes, slow ions can exist near the RPA and  $\phi_1$  should be slightly higher than the space potential. Although Eq. (1) is a good approximation to an ion beam energy from the space potential,  $E_i$  was somehow underestimated. As will be shown later, the space potential at

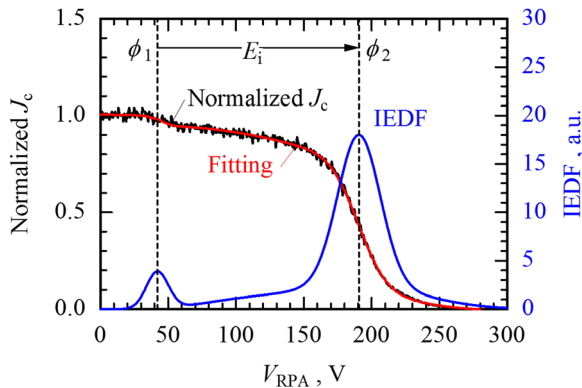


FIG. 3. Example of normalized collected ion current  $J_c$  vs third grid potential of RPA  $V_{\text{RPA}}$  with respect to cathode potential. The magnetic field was Type A with  $\dot{m}_1 = 0.41 \text{ mg/s}$  ( $=1.0 \text{ Aeq}$ ),  $\dot{m}_2 = 0.14 \text{ mg/s}$  ( $=0.36 \text{ Aeq}$ ), and  $V_d = 200 \text{ V}$ .

the RPA location under the operation condition of Fig. 3 was measured to be  $33 \text{ V}$ , which was lower than  $\phi_1$ , thereby corresponding to an underestimation of the ion beam energy by 6%.

The ion beam current  $J_i$  and ion beam divergence half-angle  $\langle \theta \rangle$  were measured using a nude Faraday probe.<sup>24</sup> The nude Faraday probe comprised a 12-mm-diameter collector and a guard ring with an inner diameter of 13 mm and an outer diameter of 23 mm. In the horizontal plane on the central axis of the DM-EST, the distribution of the ion current density,  $j_i$ , was measured as a function of the azimuthal angle,  $\theta$ , with respect to the central axis. The rotation center was  $(r, z) = (0 \text{ mm}, 115 \text{ mm})$ , and the swing arm length,  $R$ , was 250 mm. The collector part and the guard ring were negatively biased by 50 V with respect to the cathode potential, and the ion current into the collector was measured using the voltage drop at a  $1 \text{ k}\Omega$  resistor ( $\pm 1.0\%$  accuracy) connected in series to the nude Faraday probe circuit.  $j_i$  was calculated as the measured current divided by the collector area. Figure 4 shows an example of  $j_i(\theta)$  normalized by  $j_i(0)$ . Assuming an axisymmetric exhaust plume,  $J_i$  is calculated as in Eq. (2)

$$J_i = \int_{-\pi/2}^{\pi/2} j_i(\theta) \pi R^2 |\sin \theta| d\theta / (1 + \gamma). \quad (2)$$

From Fig. 3, ions with a maximum energy of  $300 \text{ eV}$  reached the collector. In this ion energy range, the secondary electron yield,  $\gamma$ , of the ion collector is approximately 0.1<sup>25</sup> and  $J_i$  was corrected by  $1 + \gamma$ . The ion beam divergence half-angle  $\langle \theta \rangle$  was calculated as the momentum-averaged value on the hemisphere face<sup>26</sup> with radius  $R$ ,

$$\cos \langle \theta \rangle = \frac{\int_{-\pi/2}^{\pi/2} j_i(\theta) |\sin \theta| \cos \theta d\theta}{\int_{-\pi/2}^{\pi/2} j_i(\theta) |\sin \theta| d\theta}. \quad (3)$$



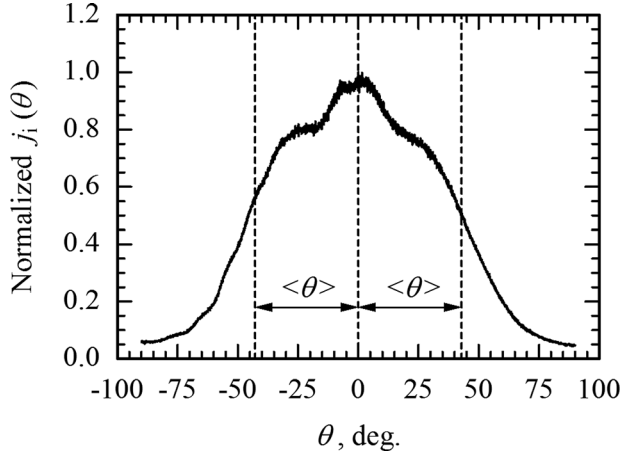


FIG. 4. Example of  $j_i(\theta)$  distribution. The magnetic field was Type C with  $\dot{m}_1 = 0.41$  mg/s ( $=1.0$  Aeq),  $\dot{m}_2 = 0.14$  mg/s ( $=0.36$  Aeq), and  $V_d = 175$  V.

The ion current measurement using a Faraday probe can make an overestimation owing to the effective collection area,<sup>27</sup> limited chamber size, and/or pumping capability.<sup>28</sup> The primary portion of uncertainty comes from charge exchange collisions between fast ions and slow neutral. Assuming a neutral temperature of 300 K and an ambient pressure of 7.6 mPa, the neutral number density is  $2.4 \times 10^{18} \text{ m}^{-3}$ . Using  $10^{-19} \text{ m}^2$  for the charge exchange collision cross-section,<sup>29</sup> the mean-free-path of charge exchange collision is on the order of  $10^{-1} \text{ m}$ . This is comparable with  $R$ , and the measured  $j_i(\theta)$  can be overestimated by charge exchange collisions. Brown<sup>30</sup> proposed seven procedures for Faraday probe measurements that can reduce the uncertainty to 3%. However, the full procedure was not performed for the data presented in this paper. Therefore, as an upper limit, the uncertainty of  $J_i$  and  $\langle\theta\rangle$  in this experiment are considered to be at the same level as those in the recent study,<sup>31</sup> and they are  $+50\%/-0\%$  and  $\pm 10\%$ , respectively.

A double probe<sup>32</sup> was used for measuring the electron number density,  $n_e$ , and the electron temperature,  $T_e$ . The probe tip comprised two 0.3-mm-diameter tungsten wires with an effective length of 3 mm. The separation distance between the tungsten wires was 2.2 mm. To obtain the probe current ( $I$ )–voltage ( $V$ ) curve, the voltage difference between the two probes was varied at 10 Hz and the probe current was measured using the same resistance as that used in the  $J_i$  measurement. The measured probe  $I$ – $V$  curve was fitted by a theoretical  $I$ – $V$  expression for a symmetric double probe<sup>32</sup>

$$I = I_{\text{sat}} \cdot \tanh\left(\frac{V}{2kT_e/e}\right) + c_1 V + c_2. \quad (4)$$

Here,  $I_{\text{sat}}$  is the ion saturation current and  $k$  is the Boltzmann constant. The coefficient  $c_1$  corresponds to the sheath expansion in the ion saturation region, and  $c_2$  reflects any offset currents owing to stray capacitance.<sup>33</sup> The parameters  $I_{\text{sat}}$ ,  $T_e$ ,  $c_1$ , and  $c_2$  are determined as fitting parameters. It should be noted that the electron energy distribution function can be a bi-Maxwellian distribution owing to the beam current from the hollow cathode. However, the double probe cannot obtain an electron temperature in the lower energy part

because it is limited to collecting the high energy tail in the electron energy distribution. Therefore, the presented  $T_e$  value indicates that the plasma contained single temperature corresponding to the higher-energy distribution. The electron number density was calculated from Eq. (5), using the Bohm approximation for the ion entry velocity to the sheath<sup>34</sup>

$$n_e = \frac{I_{\text{sat}}}{\kappa A_{\text{eff}}} \sqrt{\frac{m_i}{kT_e}}. \quad (5)$$

Here,  $\kappa$ ,  $A_{\text{eff}}$ , and  $m_i$ , are the density decrement inside pre-sheath, effective current correction area, and ion mass, respectively.  $A_{\text{eff}}$  depends on the sheath thickness  $\delta$  surrounding the probe wire, which was determined based on the Debye length<sup>35</sup> as in Eq. (6)

$$\frac{\delta}{\lambda_D} \approx \frac{2}{3} \left[ \frac{2}{\exp(-1)} \right]^{1/4} \left[ \sqrt{-\frac{1}{2} \ln\left(\frac{m_e}{m_i}\right)} - \frac{1}{\sqrt{2}} \right]^{1/2} \times \left[ \sqrt{-\frac{1}{2} \ln\left(\frac{m_e}{m_i}\right)} + \sqrt{2} \right]. \quad (6)$$

Here,  $\lambda_D$  and  $m_e$  are the Debye length and mass of electrons, respectively. For argon gas, the ratio  $\delta/\lambda_D \approx 5.0$ . In order to consider the sheath thickness,  $A_{\text{eff}}$  was initially considered to be equal to the probe surface area and an iterative process<sup>36</sup> was used.

To measure the plasma space potential,  $V_s$ , with respect to the cathode potential, a floating emissive probe<sup>37</sup> connected in parallel with a high-voltage probe (P5100A, Tektronix Company) was used. A 0.185-mm-diameter wire fabricated using 1%-thoriated tungsten was bent to a semicircular shape with a diameter of 2.0 mm and was used for thermionic electron emission. To emit a sufficient amount of thermionic electrons, the electron emission part was Joule-heated by supplying a heater current. Before the  $V_s$  measurement, the floating voltage  $V_f$  of the emissive probe was measured by varying the heater current at the ring anode inlet ( $r, z$ ) = (0 mm, 0 mm) and the exit of the accelerator ( $r, z$ ) = (0 mm, 115 mm). When a heater current greater than 5.5 A was supplied,  $V_f$  became saturated. In this condition, the voltage drop at the electron emission part was 4.5 V. Because of the space-charge effect,  $V_f$  is lower than  $V_s$ .<sup>38</sup> The measured  $V_f$  value was corrected by a factor of  $\psi_c kT_e/e$ <sup>39</sup>

$$V_s = V_f + \psi_c kT_e/e. \quad (7)$$

The correction factor  $\psi_c$  depends on the ratio of Debye length to filament radius and varies in  $0 < \psi_c < 1.5$  for argon gas. In this experiment, the heater current was fixed to 5.5 A and  $V_s$  is calculated from measured  $V_f$  and  $T_e$  values using Eq. (7).

The double probe and the emissive probe were swept using a stepping motor (PK569AWM, Oriental Motor Co., Ltd.) with a sweep time shorter than 0.25 s at each point. The probe axis was oriented parallel to the center axis of the thruster. The probe measurement position interval was at least 2 mm in the radial direction and 5 mm in the axial

direction. Because the double probe and emissive probe are used in floating voltage, the effective probe diameter  $2(r_p + \delta)$  can be calculated using Eq. (6). From the electron number density and electron temperature measurements,  $\lambda_D$  varied 0.02–0.05 mm on the central axis in the case shown in Fig. 3. The sheath thickness was 0.1–0.25 mm, and thus, the effective probe diameter was 0.5–0.8 mm. In particular, introducing probes into a bulk plasma may cause non-negligible perturbations to the thruster discharge.<sup>40,41</sup> The disturbances may influence thruster operation characteristics and plasma properties particularly around the probe location. The former effects can be characterized by discharge current  $J_d$  variation. Figure 5 shows the measured  $J_d$  value at each double probe measurement position,  $z_{\text{probe}}$ , on  $r_{\text{probe}} = 0$  and 10 mm in the Type A magnetic field. By inserting the double probe in the downstream region ( $z_{\text{probe}} > 115$  mm), the  $J_d$  difference between with and without double probe operation was smaller than 2%. The  $J_d$  difference was the largest, up to 12% (absolute value), at  $z_{\text{probe}} = 0$  mm, and then decreased towards downstream. In  $30 \text{ mm} < z_{\text{probe}} < 115$  mm, the  $J_d$  difference was 7% at most. As the probe insertion has effects on plasma properties, Staack *et al.*<sup>42</sup> reported that owing to the secondary electron emission from the probe body, the inserted probe causes an electron temperature decrement. The presented  $T_e$  value in this paper can be underestimated; however, we believe that these decrements do not have critical effects on plasma parameter distributions.

The measured values of  $n_e$ ,  $T_e$ , and  $V_s$  by probe diagnostics have uncertainties. Large combinations of effects are lumped into the uncertainties: the uncertainty of electrode collection area,<sup>43</sup> finite ion temperature,<sup>44</sup> noise in the collected signal, and applicability of the probe theory.<sup>45</sup> As mentioned earlier,  $I_{\text{sat}}$  and  $T_e$  are determined directly as fitting parameters in Eq. (4). The standard deviation of  $T_e$  fitting was up to 15%. The uncertainty of  $n_e$  is the combination of the uncertainty of each parameter in Eq. (5), that is, the standard deviation of  $I_{\text{sat}}$  fitting, finite ion temperature effect on  $\kappa$ , probe manufacturing accuracy on  $A_{\text{eff}}$ , and  $T_e$  uncertainty. Applying the low propagation of error in Eq. (5), the estimated  $n_e$  uncertainty was +13%/–16% which is the maximum. From Eq. (7), the uncertainty of  $V_s$  is of the same

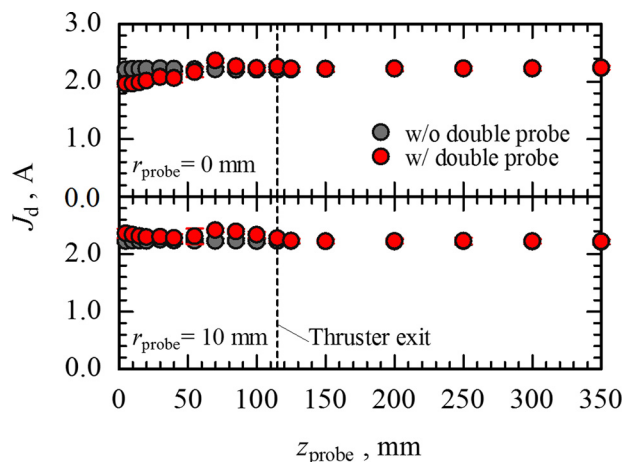


FIG. 5. Probe perturbation on  $J_d$  with the magnetic field of Type A with  $\dot{m}_1 = 0.41 \text{ mg/s}$  ( $=1.0 \text{ Aeq}$ ),  $\dot{m}_2 = 0.14 \text{ mg/s}$  ( $=0.36 \text{ Aeq}$ ), and  $V_d = 200 \text{ V}$ .

order as the uncertainty of  $T_e$ . However, Eq. (7) neglects the potential drop in the pre-sheath region.<sup>46</sup> In the typical operation condition of Hall thrusters, the pre-sheath thickness is comparable with that of the discharge channel width, that is, 20 mm.<sup>7</sup> This is comparable with that of the ring anode inner diameter. Moreover, the heating current flows in the emission probe make 4.5 V of the potential drop in the emission part. Therefore, the uncertainty of  $V_s$  is  $+0.15\psi_c(kT_e/e)/-0.9(kT_e/e) \pm 2.25 \text{ V}$ .

### III. ION ACCELERATION CHARACTERISTICS

#### A. Operating conditions

All experiments were conducted in a 3.2-m-long, 1.2-m-diameter stainless steel vacuum chamber. The vacuum chamber was evacuated using a cryogenic pump with an exhaust speed of 8400 l/s, which was backed by a dry pump with an exhaust speed of 120 l/s. The working gas supplied both through the slit and through the hollow cathode was argon (purity 99.9999%). The flow rate of the working gas injected through the slit,  $\dot{m}_1$ , was set to 0.41 mg/s ( $=1.0 \text{ Aeq}$ ), and the discharge voltage  $V_d$  ranged from 125 V to 225 V. Here, the unit for flow rate “Aeq” stands for “ampere equivalent,” which is frequently used in evaluating thrust characteristics of an electrostatic thruster.<sup>47</sup> One Aeq corresponds to a flow rate of propellant particles multiplied by an elementary charge. The hollow cathode was operated with a working gas flow rate,  $\dot{m}_2$ , of 0.14 mg/s ( $=0.36 \text{ Aeq}$ ), and the keeper current was fixed to 2.0 A. The ambient pressure in the vacuum chamber, measured using an ionization gauge, was maintained below 7.6 mPa with the total working gas flow rate of 0.55 mg/s ( $=1.36 \text{ Aeq}$ ). Each operating condition was repeated at least twice with measuring  $E_i$ ,  $J_i$ ,  $\langle \theta \rangle$ ,  $J_d$ , and the keeper voltage. In the following figures, a symbol shows an average value. The error bar in  $E_i$ ,  $J_i$ ,  $J_d$ , and  $\langle \theta \rangle$  correspond to the standard deviation ( $\pm \sigma$ ) obtained by a number of trials. Each steady-state operation to measure the thrust characteristics lasted for at least 3.5 s. To evaluate the effect of the insulating plate erosion, the insulating plate mass was measured using an electric balance (AW320, Shimadzu Corp.) before and after five operation cycles (10 s run and 30 s interval) at the condition  $\dot{m}_1 = 0.41$  ( $=1.0 \text{ Aeq}$ ) mg/s,  $\dot{m}_2 = 0.14$  mg/s ( $=0.36 \text{ Aeq}$ ), and  $V_d = 200 \text{ V}$  in the Type A magnetic field. The mass difference before and after operation was smaller than the resolution of the electric balance (0.1 mg), which corresponds to a value not greater than  $2 \mu\text{g/C}$ .

#### B. Effect of magnetic field strength

In this section, the effect of the magnetic field strength is examined by comparing the ion beam characteristics of Types N and S, both of which had a relatively uniform applied magnetic field. Figure 6(a) shows the  $j_i(\theta)$  distribution in Types N and S. In both Types N and S, more than 175 V of discharge voltage was necessary for breakdown and steady-state operation. In Type N,  $j_i(\theta)$  exhibits a local peak at  $\theta = 0^\circ$  and  $\pm 50^\circ$ . However, in Type S,  $j_i(\theta)$  exhibits a maximum only around  $\theta = 0^\circ$  and then monotonically decreases with increasing  $|\theta|$ . As a result, as shown in Fig. 6(b), the  $\langle \theta \rangle$  value

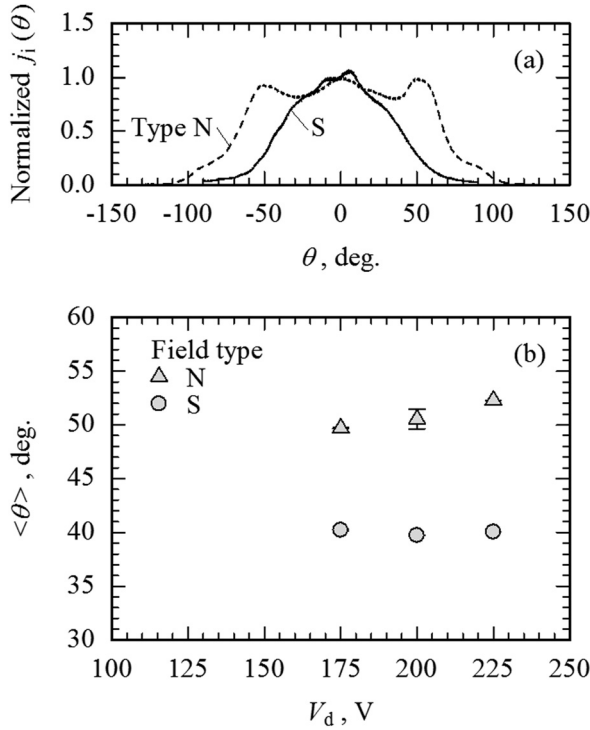


FIG. 6. Ion beam distribution characteristics in Type N and S magnetic fields, where  $\dot{m}_1 = 0.41$  mg/s ( $=1.0$  Aeq) and  $\dot{m}_2 = 0.14$  mg/s ( $=0.36$  Aeq); (a) normalized ion beam current density  $j_i$  vs. angle  $\theta$  with respect to the central axis for  $V_d = 200$  V, (b)  $\langle \theta \rangle$  vs.  $V_d$ .

of Type S was smaller than that of Type N by more than  $10^\circ$ ; for example, at  $V_d = 225$  V,  $\langle \theta \rangle$  is  $52^\circ$  and  $40^\circ$  for Types N and S, respectively. In the case of Type N,  $\langle \theta \rangle$  increased by  $3^\circ$  with increasing  $V_d$  from 175 to 225 V. However, in Type S, it varied by not greater than  $1^\circ$ .

Figure 7 shows the  $V_d$  dependence of  $E_i$ ,  $J_i$ , and  $J_d$  for Types N and S. In both types, the average value of  $E_i$  increased almost linearly with increasing  $V_d$ . In the steady-state operation region ( $V_d \geq 175$  V), the slope  $dE_i/dV_d$  was 0.65 for Type N and 1.0 for Type S. At  $V_d = 225$  V,  $J_i$  was 87% and 100% of the total working gas flow rate in ampere equivalent  $e(\dot{m}_1 + \dot{m}_2)/m_i$  for Types N and S, respectively. In the latter, ion production by magnetized electrons was enhanced owing to the better confinement achieved by the stronger magnetic field. In both types, with increasing  $V_d$ ,  $J_i$  almost became saturated to a value equal to  $e(\dot{m}_1 + \dot{m}_2)/m_i$ . As shown in Fig. 7,  $J_d$  increased with the stronger magnetic field of Type S, at  $V_d = 225$  V and  $J_d = 2.1$  A and 2.6 A for Types N and S, respectively. Additionally,  $J_d$  increased with increasing  $V_d$  in both types—however, without saturation—and surpassed  $e\dot{m}_1/m_i$  by a factor of 2 or higher.  $J_d$  equals the electron current flowing into the ring anode, which is the sum of the exhaust ion current that should be neutralized by electrons and an “excess” electron current owing to the diffusion of thermionic electrons, which is equivalent to the electron backflow from the hollow cathode. Because  $J_i$  saturated with increasing  $V_d$  while  $J_d$  increased monotonically, the ratio  $J_i/J_d$  exhibited a maximum value, which in the present configuration was 0.67 for both types; 67% of  $J_d$  corresponds to the ion current and the rest to the electron backflow. In Type N,  $J_i/J_d$  exhibited a peak value at  $V_d = 200$  V, and in

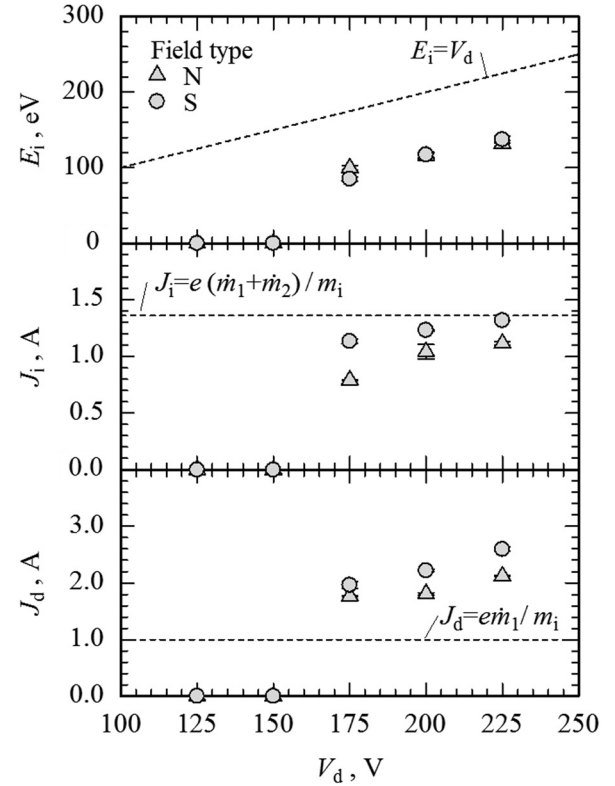


FIG. 7.  $V_d$  vs.  $E_i$ ,  $J_i$ , and  $J_d$  for Type N and S magnetic fields with  $\dot{m}_1 = 0.41$  mg/s ( $=1.0$  Aeq) and  $\dot{m}_2 = 0.14$  mg/s ( $=0.36$  Aeq).

Type S, it had a maximum at  $V_d = 175$  V and decreased monotonically with increasing  $V_d$ .

### C. Effect of magnetic field distribution

In this section, the operation characteristics of Types A and C are compared to those of Type S to evaluate the effect of the magnetic field distribution. Figure 8(a) shows the  $j_i(\theta)$  distribution for Types S, A, and C. Only in Type A, breakdown and steady-state operation were possible at a low discharge voltage, as low as  $V_d = 125$  V. In Type A,  $j_i(\theta)$  had local maxima at  $\theta = \pm 10^\circ$  that were 5%–10% higher than  $j_i(0)$ . In Type C, similar to Type S,  $j_i(\theta)$  exhibited a peak value only at the central axis, at  $\theta = 0^\circ$ . Fig. 8(b) shows the  $V_d$  dependence of  $\langle \theta \rangle$  in Types S, A, and C. In contrast to Type S, the  $\langle \theta \rangle$  value of Type C increased with increasing  $V_d$ ; however, in Type A, it decreased. Among the types examined in this study, Type A exhibited the smallest  $\langle \theta \rangle$ , which was  $39^\circ$  at  $V_d = 225$  V. Figure 9 shows the  $V_d$  dependence of  $E_i$ ,  $J_i$ , and  $J_d$  for Types S, A, and C. In Types A and C, with increasing  $V_d$ ,  $E_i$  increased almost linearly with the same increasing rate as Type S,  $dE_i/dV_d \approx 1.0$  in the steady-state operation region ( $V_d \geq 175$  V for Type C and  $V_d \geq 150$  V for Type A). When  $V_d$  was in the range of 175–225 V,  $E_i$  of Type C differed from that of Type S by not more than 8%. However, in Type A,  $E_i$  was approximately 40 eV higher than that of Type S, and at  $V_d = 225$  V,  $E_i/V_d$  reached 0.79. No clear difference was observed in the variation in  $J_i$  among Types S, A, and C; at  $V_d = 225$  V,  $J_i$  saturated at a value slightly higher than  $e(\dot{m}_1 + \dot{m}_2)/m_i$ . The cause for this excess value has not been clearly identified; it could

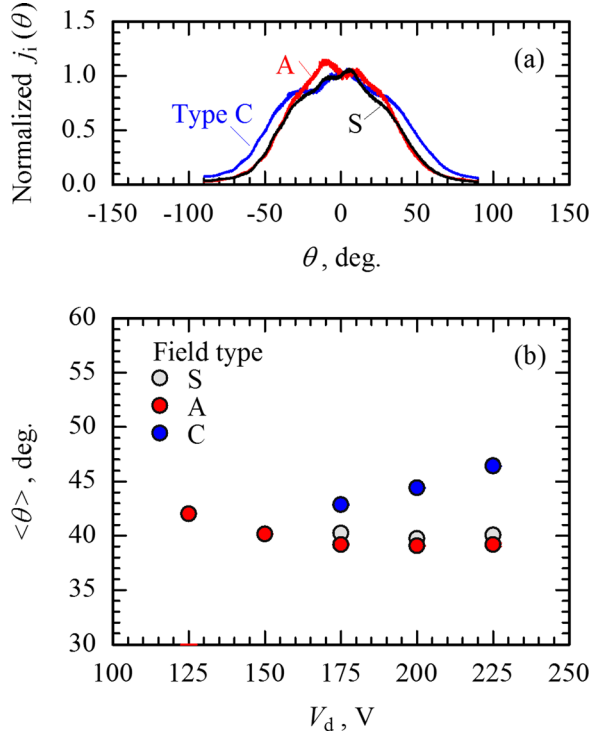


FIG. 8. Ion beam distribution characteristics for Type S, A, and C magnetic fields with  $\dot{m}_1 = 0.41$  mg/s ( $=1.0$  Aeq) and  $\dot{m}_2 = 0.14$  mg/s ( $0.36$  Aeq); (a) normalized ion beam current density  $j_i$  vs. angle  $\theta$  with respect to the central axis for  $V_d = 200$  V and (b)  $\langle \theta \rangle$  vs.  $V_d$ .

be due to the failure of the symmetry, doubly charged ions, or other reasons. However, the conclusions obtained from the present experiments are not expected to be affected by this small discrepancy. In both Types A and C,  $J_d$  increased without saturation and then  $J_i/J_d$  decreased with increasing  $V_d$ .

#### IV. DISCUSSION ON ION ACCELERATION MECHANISMS BASED ON PROBE DIAGNOSTICS

In this section, the probe diagnostics results are used for analyzing the ion acceleration and discharge characteristics discussed in Sec. III.

##### A. Ionization characteristics

As shown in Figs. 7 and 9, in Types S, A, and C,  $J_i$  was 18%–25% higher than that of Type N, which indicates that  $J_i$  increases with increasing  $B$ . Figure 10 shows the  $n_e$  distribution for each magnetic field type. With a strong magnetic field, in Types S, A, and C,  $n_e$  on the central axis inside the ring anode was of the order of  $10^{18} \text{ m}^{-3}$ . In Type C,  $n_e$  exhibited a local peak value of  $1.8 \times 10^{18} \text{ m}^{-3}$  at  $(r, z) = (0 \text{ mm}, 40 \text{ mm})$ .

Figure 11 shows the radial distributions of  $n_e$ ,  $T_e$ , and  $V_s$  at  $z = 10$  mm, near the right-hand-side end of the ring anode. In Type N, with a relatively weak magnetic field of 100 mT,  $n_e$  remained at a low level of up to  $2 \times 10^{17} \text{ m}^{-3}$  for  $r \leq 8$  mm; however, at  $r = 10$  mm, it increased up to  $2 \times 10^{18} \text{ m}^{-3}$ . As was reported in Ref. 18, the neutral gas injected through the annular slit along the anode inner surface was efficiently ionized by electrons diffusing into the anode across a potential drop exceeding the ionization energy. Because the ions so

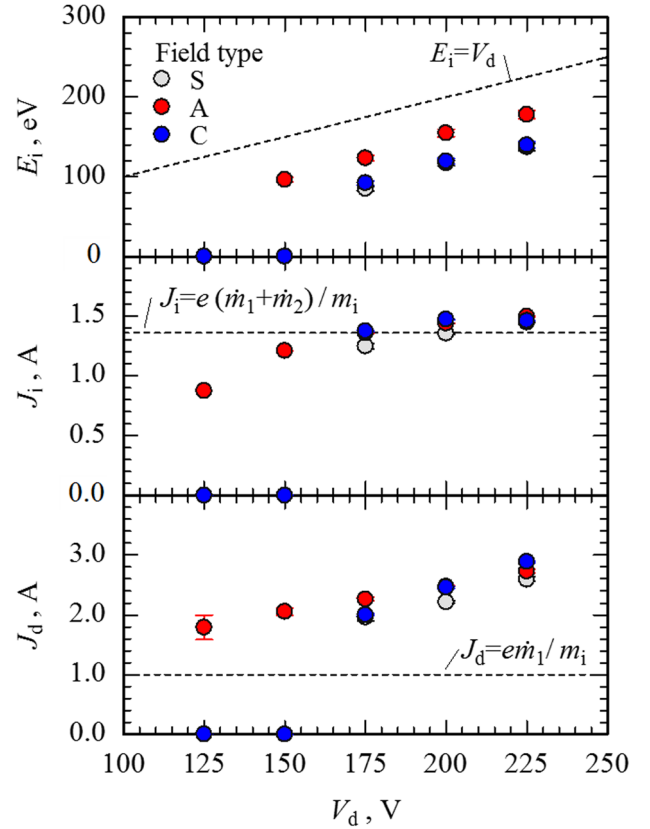


FIG. 9.  $V_d$  vs.  $E_i$ ,  $J_i$ , and  $J_d$  for Type S, A, and C magnetic fields with  $\dot{m}_1 = 0.41$  mg/s ( $=1.0$  Aeq) and  $\dot{m}_2 = 0.14$  mg/s ( $=0.36$  Aeq).

ionized in this region can be accelerated over the potential drop that is almost equal to the discharge voltage, this scheme is favorable for the electrostatic acceleration. This scheme will hereafter be referred to as the “near-anode ionization scheme.”

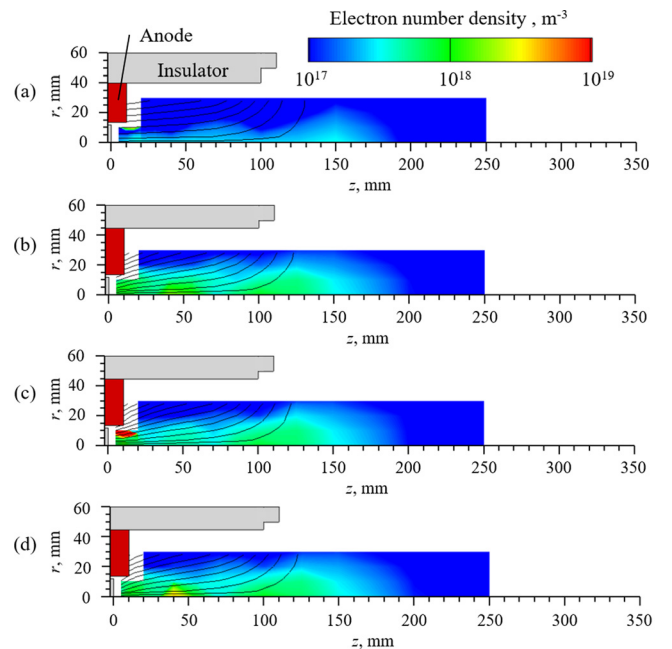


FIG. 10. Distributions of  $n_e$  for varying magnetic field types: (a) Type N, (b) Type S, (c) Type A, and (d) Type C, with  $\dot{m}_1 = 0.41$  mg/s ( $=1.0$  Aeq),  $\dot{m}_2 = 0.14$  mg/s ( $=0.36$  Aeq), and  $V_d = 200$  V.



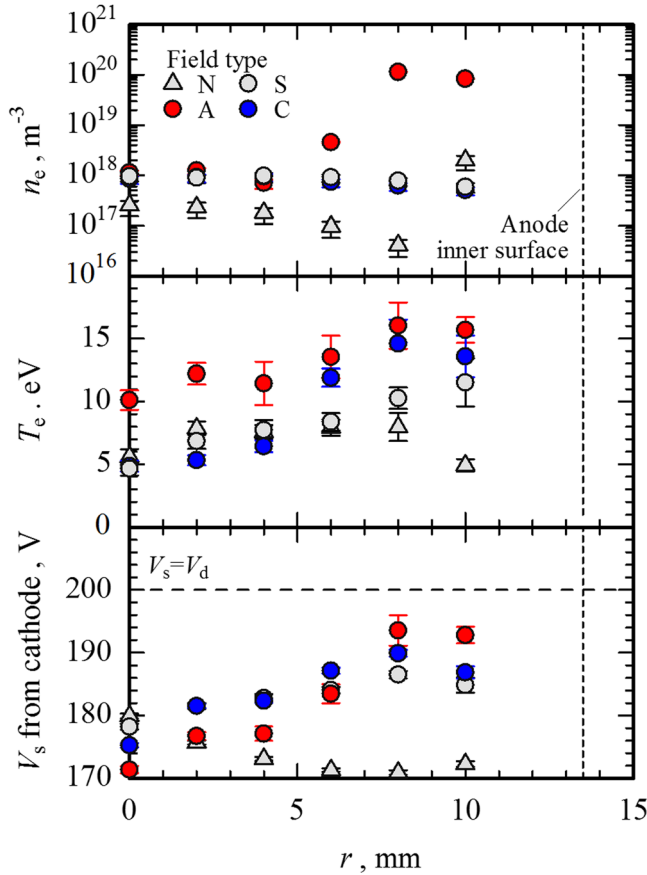


FIG. 11. Distributions of  $n_e$ ,  $T_e$ , and  $V_s$  at  $z = 10$  mm for various magnetic field types, with  $\dot{m}_1 = 0.41$  mg/s ( $=1.0$  Aeq),  $\dot{m}_2 = 0.14$  mg/s ( $=0.36$  Aeq), and  $V_d = 200$  V.

In all other locations,  $n_e$  was higher in Types S and C than in Type N, ranging between  $5.0 \times 10^{17}$  and  $1.0 \times 10^{18} \text{ m}^{-3}$  in the entire  $r$  range. In Type A,  $n_e$  was at the same level as in Types S and C for  $r \leq 4$  mm and then increased up to  $1.0 \times 10^{20} \text{ m}^{-3}$  at  $r = 8$  and  $10$  mm.

In Types N, S, and C,  $T_e$  was approximately  $5.0$  eV and increased slowly with increasing  $r$ . In Type N,  $T_e$  decreased at  $r = 10$  mm, which corresponds to the increment of  $n_e$ . In Type S,  $T_e$  continued to increase with increasing  $r$ . In Type A,  $T_e$  remained at the highest level of  $10$ – $16$  eV. In Type C,  $T_e$  increased to the same level as Type A at  $r = 8$  mm; as shown in Fig. 10, only Type A had a region of considerably high  $n_e$  of the order of  $1 \times 10^{19} \text{ m}^{-3}$  near the inner surface of the ring anode.

In Type N,  $V_s$  at  $z = 10$  mm decreased with increasing  $r$  from  $179$  V at the center to  $170$  V at  $r = 10$  mm. In Types S, A, and C, which had a stronger magnetic field,  $V_s$  increased from the axis to the ring anode inner surface because of the decreasing electron's mobility perpendicular to the magnetic lines of force; in Type A,  $V_s$  is the lowest at the central axis with a value of  $171$  V, which is lower than the anode potential ( $=V_d$ ) by  $29$  V. This potential difference is sufficient for the thermionic electrons at the central axis to enhance ionization near the ring anode inner surface. In particular, in Types A and C,  $T_e$  exceeded the ionization energy of argon ( $=15.8$  eV) in the  $r = 8$ – $10$  mm region. In this electron temperature region, the ionization rate constant strongly depends

on  $T_e$ . The working gas injected through the injection slit collided with energetic electrons at a high rate, thereby enhancing ionization; Types S, A, and C exhibited more than  $10$  times higher electron number density. Particularly for Type A, combining the near-anode ionization scheme with the strengthened magnetic field and the potential drop, electron impact ionization probability increased so that a high  $n_e$  region of the order of  $10^{20} \text{ m}^{-3}$  was formed near the anode inner surface. This scenario is favorable for the efficient electrostatic acceleration of ions almost equivalent to the total working gas flow rate through a potential drop close to  $V_d$ .

## B. Acceleration characteristics

As shown in Figs. 6(b) and 8(b),  $\langle \theta \rangle$  depended on both the strength and the profile of the applied magnetic field. Particularly,  $\langle \theta \rangle$  decreased in the order of Types N, C, S, and A. Figure 12 shows color contours of  $T_e$  for all types. Each  $T_e$  distribution exhibited a peak in the diverging part of the applied magnetic field. In Type N,  $T_e$  exhibited a maximum of approximately  $34$  eV near the central axis at  $z = 100$  mm. In Types S, A, and C, a maximum  $T_e$  of approximately  $30$  eV appeared upstream, at approximately  $z = 55$ – $85$  mm. Figure 13 shows the distributions of  $n_e$ ,  $T_e$ , and  $V_s$  on the central axis. In the region near a maximum  $T_e$ ,  $V_s$  started to decrease in the downstream direction. In Type N,  $V_s$  started to decrease at approximately  $z = 100$  mm, where  $T_e$  exhibited a maximum. However, in the other types, which had a stronger magnetic field,  $V_s$  started to decrease at  $z = 70$ – $80$  mm. These results suggest that increasing the magnetic field results in shifting the location of the ion acceleration region toward the ring anode. Figure 14 shows the color contours of  $V_s$  for all the examined magnetic field types. By strengthening the magnetic field, as in Types S, A, and C, an electric field oriented obliquely inward.

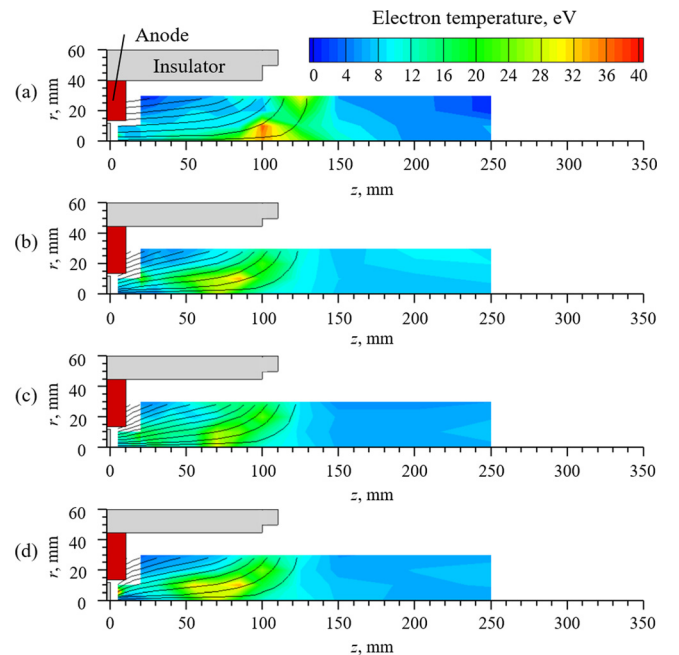


FIG. 12. Distributions of  $T_e$  for various magnetic field types: (a) Type N, (b) Type S, (c) Type A, and (d) Type C, with  $\dot{m}_1 = 0.41$  mg/s ( $=1.0$  Aeq),  $\dot{m}_2 = 0.14$  mg/s ( $=0.36$  Aeq), and  $V_d = 200$  V.

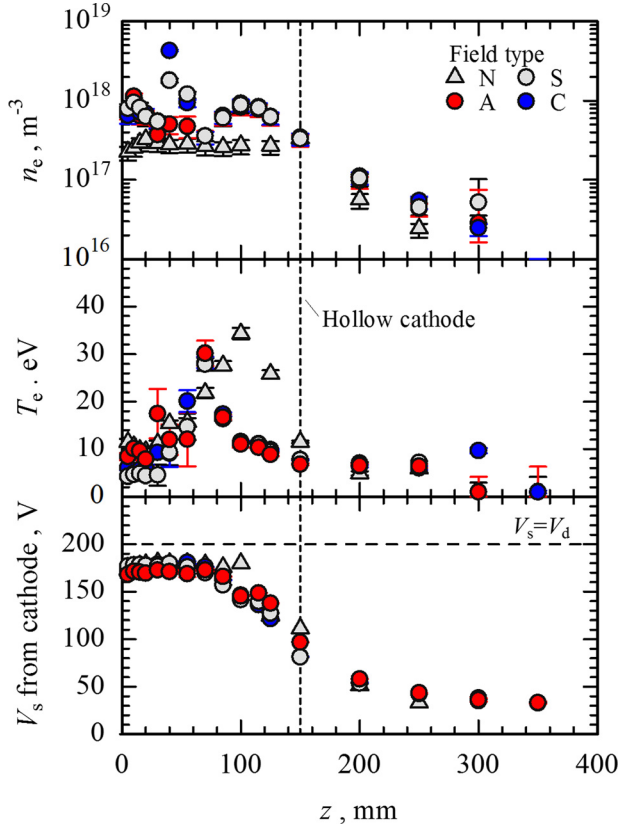


FIG. 13. Distributions of  $n_e$ ,  $T_e$ , and  $V_s$  on the central axis for various magnetic field types with  $\dot{m}_1 = 0.41 \text{ mg/s}$  ( $=1.0 \text{ Aeq}$ ),  $\dot{m}_2 = 0.14 \text{ mg/s}$  ( $=0.36 \text{ Aeq}$ ), and  $V_d = 200 \text{ V}$ .

This electric field collimated ions, thereby decreasing the  $\langle \theta \rangle$  value of Types S, A, and C with respect to that of Type N. The strength of this electric field depended on the space potential distribution and resulted in a lowered space potential at the

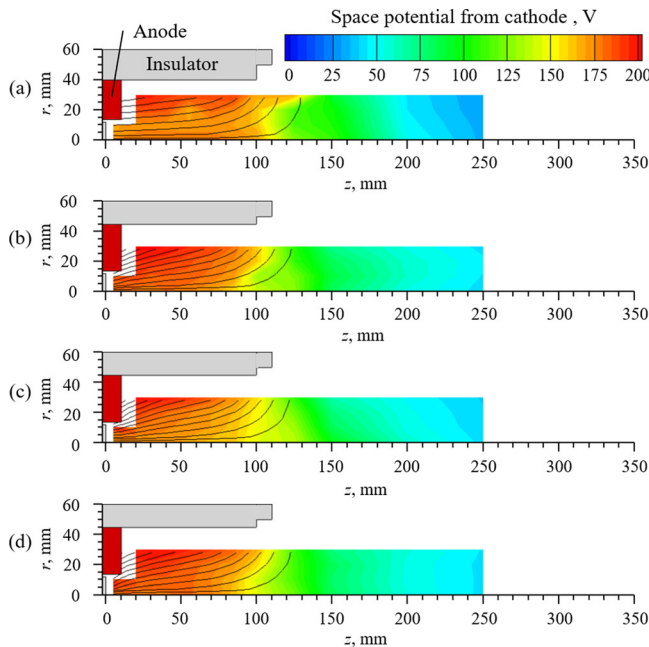


FIG. 14. Distributions of  $V_s$  for various magnetic field types: (a) Type N, (b) Type S, (c) Type A, and (d) Type C, with  $\dot{m}_1 = 0.41 \text{ mg/s}$  ( $=1.0 \text{ Aeq}$ ),  $\dot{m}_2 = 0.14 \text{ mg/s}$  ( $=0.36 \text{ Aeq}$ ), and  $V_d = 200 \text{ V}$ .

central axis. As shown in Fig. 13, Type A exhibited the lowest space potential at the central axis for  $z = 0\text{--}55 \text{ mm}$  and the smallest  $\langle \theta \rangle$ .

As described by Eq. (1), the ion energy  $E_i$  of electrostatic acceleration was determined from the space potential difference from the ionization position (see  $\phi_2$  in Fig. 3) to the IEDF measurement position (see  $\phi_1$  in Fig. 3). As shown in Figs. 7 and 9, Type A exhibited the highest  $E_i$ ; on the other hand, the difference in  $E_i$  between Types N, S, and C was not higher than 5 eV. In Type A, ionization was enhanced locally near the ring anode inner surface, as shown in Fig. 10. The measured  $V_s$  at  $(r, z) = (10 \text{ mm}, 10 \text{ mm})$  was 192 V, close to the  $\phi_2$  value ( $=190 \text{ V}$ ) measured by the RPA. In Types N, S, and C,  $n_e$  exhibited maxima of 172, 179, and 179 V at  $(r, z) = (10 \text{ mm}, 10 \text{ mm})$ ,  $(0 \text{ mm}, 40 \text{ mm})$ , and  $(0 \text{ mm}, 40 \text{ mm})$ , respectively. As shown in Fig. 13, at the IEDF measurement position  $(r, z) = (0 \text{ mm}, 350 \text{ mm})$ ,  $V_s$  was almost equal for all magnetic field types. Therefore,  $E_i$  mainly depends on  $V_s$  at the ionization position. In Type A, the enhanced ionization near the ring anode potential, induced by the combination of the near-anode ionization scheme with the strengthened magnetic field, can make the electrostatic ion acceleration more efficient.

## V. CONCLUSION

In this study, we investigated the magnetic field types in a DM-EST and concluded that Type A, in which the applied magnetic field is locally strengthened on the ring anode inner surface, exhibited the highest ion beam energy and the smallest beam divergence of  $39^\circ$  because of enhanced ionization near the ring anode inner surface owing to the combination of the near-anode ionization scheme with the strengthened magnetic field. In the acceleration region, an obliquely inward electric field converted ions to the central axis, thereby mitigating the ion collisions against the channel wall. Subsequently, the ions were accelerated through a potential drop in the axial direction. With such favorable ion acceleration characteristics, DM-EST is expected to be useful as another type of electrostatic acceleration device for in-space electric propulsion.

## ACKNOWLEDGMENTS

This research was supported by JSPS KAKENHI Grant No. JP15H02321. The authors thank A. Saito at the Technical Division, Nagoya University, for his valuable technical assistance.

<sup>1</sup>D. Y. Oh, J. S. Snyder, D. M. Goebel, R. R. Hofer, and T. M. Randolph, "Solar electric propulsion for Discovery-class missions," *J. Spacecr. Rockets* **51**, 1822–1835 (2014).

<sup>2</sup>D. M. Goebel and I. Katz, *Fundamentals of Electric Propulsion: Ion and Hall Thrusters* (John Wiley & Sons, 2008), pp. 429–446.

<sup>3</sup>J. Snyder, D. M. Goebel, R. R. Hofer, J. E. Polk, N. C. Wallace, and H. Simpson, "Performance evaluation of the T6 ion engine," *J. Propul. Power* **28**, 371–379 (2012).

<sup>4</sup>C. D. Child, "Discharge from hot  $\text{CaO}$ ," *Phys. Rev. (Series I)* **32**, 492–511 (1911).

<sup>5</sup>I. Langmuir, "The effect of space charge and initial velocities on the potential distribution and thermionic current between parallel plane electrodes," *Phys. Rev.* **21**, 419–435 (1923).

<sup>6</sup>J.-P. Boeuf, "Tutorial: Physics and modeling of Hall thrusters," *J. Appl. Phys.* **121**, 011101 (2017).

- <sup>7</sup>M. Keidar, I. D. Boyd, and I. I. Beilis, "Plasma flow and plasma-wall transition in Hall thruster channel," *Phys. Plasmas* **8**, 5315–5322 (2001).
- <sup>8</sup>S. Qing, P. E. Guangqing Xia, M.-C. Tang, and P. Duan, "Optimized electrode placement along the channel of a Hall thruster for ion focusing," *J. Appl. Phys.* **115**, 033301 (2014).
- <sup>9</sup>I. G. Mikellides, I. Katz, R. R. Hofer, and D. M. Goebel, "Magnetic shielding of a laboratory Hall thruster. I. Theory and validation," *J. Appl. Phys.* **115**, 043303 (2014).
- <sup>10</sup>S. Mazouffre, S. Tskikata, and J. Vaudolon, "Development and experimental characterization of a wall-less Hall thruster," *J. Appl. Phys.* **116**, 243302 (2014).
- <sup>11</sup>J. Vaudolon, S. Mazouffre, C. Hénau, D. Hamibey, and A. Rossi, "Optimization of a wall-less Hall thruster," *Appl. Phys. Lett.* **107**, 174103 (2015).
- <sup>12</sup>K. D. Diamant, J. E. Pollard, Y. Raitses, and N. J. Fisch, "Ionization, plume properties, and performance of cylindrical Hall thrusters," *IEEE Trans. Plasma Sci.* **38**, 1052–1057 (2010).
- <sup>13</sup>N. Koch, H. P. Harmann, and G. Kornfeld, "Development and test status of the THALES high efficiency multistage plasma (HEMP) thruster family," in *Proceedings of the 29th International Electric Propulsion Conference, Princeton, USA* (2005), IEPC Paper No. 2005–297.
- <sup>14</sup>N. A. MacDonald, C. V. Young, M. A. Cappelli, and W. A. Hargus, Jr., "Ion velocity and plasma potential measurements of a cylindrical cusped field thruster," *J. Appl. Phys.* **111**, 093303 (2012).
- <sup>15</sup>T. S. Matlock, Ph.D thesis, Massachusetts Institute of Technology, 2012.
- <sup>16</sup>S. Harada, T. Baba, A. Uchigashima, S. Yokota, A. Iwakawa, A. Sasoh, T. Yamazaki, and H. Shimizu, "Electrostatic acceleration of helicon plasma using a cusped magnetic field," *Appl. Phys. Lett.* **105**, 194101 (2014).
- <sup>17</sup>A. Uchigashima, T. Baba, D. Ichihara, A. Iwakawa, A. Sasoh, T. Yamazaki, S. Harada, M. Sasahara, and T. Iwasaki, "Anode geometry effects on ion beam energy performance in helicon electrostatic thruster," *IEEE Trans. Plasma Sci.* **44**, 306–313 (2016).
- <sup>18</sup>D. Ichihara, A. Uchigashima, A. Iwakawa, and A. Sasoh, "Electrostatic ion acceleration across a diverging magnetic field," *Appl. Phys. Lett.* **109**, 053901 (2016).
- <sup>19</sup>J. E. Foster and A. D. Gallimore, "The effect of an auxiliary discharge on anode sheath potentials in a transverse discharge," *J. Appl. Phys.* **81**, 3422–3432 (1997).
- <sup>20</sup>A. Anders and S. Andres, "The working principle of the hollow-anode plasma source," *Plasma Source Sci. Technol.* **4**, 571–575 (1995).
- <sup>21</sup>H. R. Kaufman, R. S. Robinson, and R. I. Seddon, "End-Hall ion source," *J. Vac. Sci. Technol.* **5**, 2081–2084 (1987).
- <sup>22</sup>N. Oudini, G. J. Hagelaar, J.-P. Boeuf, and L. Garrigues, "Physics and modeling of an end-Hall (gridless) ion source," *J. Appl. Phys.* **109**, 073310 (2011).
- <sup>23</sup>J. A. Simpson, "Design of retarding field energy analyzers," *Rev. Sci. Instrum.* **32**, 1283–1293 (1961).
- <sup>24</sup>M. L. R. Walker, R. R. Hofer, and A. D. Gallimore, "Ion collection in Hall thruster plumes," *J. Propul. Power* **22**, 205–209 (2006).
- <sup>25</sup>H. D. Hagstrum, "Auger ejection of electrons from tungsten by noble gas ions," *Phys. Rev.* **96**, 325–335 (1954).
- <sup>26</sup>D. L. Brown, C. W. Larson, B. E. Beal, and A. D. Gallimore, "Methodology and historical perspective of a Hall thruster efficiency analysis," *J. Propul. Power* **25**, 1163–1177 (2009).
- <sup>27</sup>D. L. Brown and A. D. Gallimore, "Evaluation of ion collection area in Faraday probes," *Rev. Sci. Instrum.* **81**, 063504 (2010).
- <sup>28</sup>D. Kusamoto, K. Mikami, K. Komurasaki, and A. D. Gallimore, "Exhaust beam profiles of Hall thruster," *Trans. Japan Soc. Aero. Space Sci.* **40**, 238–247 (1998).
- <sup>29</sup>M. V. V. S. Rao, R. J. Van Brunt, and J. K. Olthoff, "Resonant charge exchange and the transport of ions at high electric-field to gas-density ratios (E/N) in argon, neon, and helium," *Phys. Rev. E* **54**, 5641–5656 (1996).
- <sup>30</sup>D. L. Brown, Ph.D thesis, University of Michigan, 2009.
- <sup>31</sup>K. G. Xu and M. L. Walker, "Plume characterization of an ion-focusing Hall thruster," *J. Propul. Power* **28**, 1105–1115 (2012).
- <sup>32</sup>E. O. Johnson and L. Malter, "A floating double probe method for measurements in gas discharge," *Phys. Rev.* **80**, 58–70 (1950).
- <sup>33</sup>B. A. Smith and L. J. Overzet, "Improvements to the floating double probe for time-resolved measurements in pulsed rf plasmas," *Rev. Sci. Instrum.* **69**, 1372–1377 (1998).
- <sup>34</sup>P. Chung, "Electrostatic probes in stationary and flowing plasmas: Part 1. Collisionless and transitional probes," *AIAA J.* **12**, 133–144 (1974).
- <sup>35</sup>I. H. Hutchinson, *Principles of Plasma Diagnostics*, 2nd ed. (Cambridge University Press, 2002), pp. 65–67.
- <sup>36</sup>J. M. Hass and A. D. Gallimore, "Considerations on the role of the Hall current in a laboratory-model thruster," *IEEE Trans. Plasma Sci.* **30**, 687–697 (2002).
- <sup>37</sup>J. P. Sheehan and N. Hershkowitz, "Emissive probes," *Plasma Sources Sci. Technol.* **20**, 063001 (2011).
- <sup>38</sup>J. P. Sheehan, Y. Raitses, N. Hershkowitz, I. Kaganovich, and N. J. Fisch, "A comparison of emissive probe techniques for electric potential measurements in a complex plasma," *Phys. Plasmas* **18**, 073501 (2011).
- <sup>39</sup>A. Fruchtman, D. Zoler, and G. Makrinich, "Potential of an emissive cylindrical probe in plasma," *Phys. Rev. E* **84**, 025402 (2011).
- <sup>40</sup>D. Yordanov, S. Lishev, and A. Shivarova, "How does a probe inserted into the discharge influence the plasma structure?," *J. Appl. Phys.* **119**, 183302 (2016).
- <sup>41</sup>Y. Raitses, M. Keidar, D. Staack, and N. J. Fisch, "Effects of segmented electrode in Hall current plasma thrusters," *J. Appl. Phys.* **92**, 4906–4911 (2002).
- <sup>42</sup>D. Staack, Y. Raitses, and N. J. Fisch, "Shielded electrostatic probe for nonperturbing plasma measurements in Hall thrusters," *Rev. Sci. Instrum.* **75**, 393–399 (2004).
- <sup>43</sup>T. E. Sheridan, "How big is a small Langmuir probe?," *Phys. Plasmas* **7**, 3084–3088 (2000).
- <sup>44</sup>G. A. Emmert, R. M. Wieland, A. T. Mense, and J. N. Davidson, "Electric sheath and presheath in a collisionless, finite ion temperature plasma," *Phys. Fluids* **23**, 803–812 (1980).
- <sup>45</sup>D. A. Herman and A. D. Gallimore, "An ion thruster internal discharge chamber electrostatic probe diagnostics technique using high-speed probe positioning system," *Rev. Sci. Instrum.* **79**, 013302 (2008).
- <sup>46</sup>L. A. Schwager, "Effects of secondary and thermionic electron emission on the collector and source sheaths of a finite ion temperature plasma using kinetic theory and numerical simulation," *Phys. Fluids B* **5**, 631–645 (1993).
- <sup>47</sup>P. George, *Sutton and Oscar Biblarz, Rocket Propulsion Elements* (John Wiley & Sons, 2000), p. 681.